Automatic Detection of Regional Heart Rejection in USPIO-Enhanced MRI

Hsun-Hsien Chang, José M. F. Moura, *Fellow, IEEE*,
Yijen L. Wu, and Chien Ho

Abstract

Contrast-enhanced magnetic resonance imaging (MRI) is useful to study the infiltration of cells *in vivo*. This research adopts ultrasmall superparamagnetic iron oxide (USPIO) particles as contrast agents. USPIO particles administered intravenously can be endocytosed by circulating immune cells, in particular, macrophages. Hence, macrophages are labeled with USPIO particles. When a transplanted heart undergoes rejection, immune cells will infiltrate the allograft. Imaged by T_2^*-weighted MRI, USPIO-labeled macrophages display dark pixel intensities. Detecting these labeled cells in the image facilitates the identification of acute heart rejection.

This paper develops a classifier to detect the presence of USPIO-labeled macrophages in the myocardium in the framework of spectral graph theory. First, we describe a USPIO-enhanced heart image with a graph. Classification becomes equivalent to partitioning the graph into two disjoint subgraphs. We use the Cheeger constant of the graph as an objective functional to derive the classifier. We represent the classifier as a linear combination of basis functions given from the spectral analysis of the graph Laplacian. Minimization of the Cheeger constant based functional leads to the optimal classifier. Experimental results and comparisons with other methods suggest the feasibility of our approach to study the rejection of hearts imaged by USPIO-enhanced MRI.

Index Terms

Cardiac magnetic resonance imaging (cardiac MRI), USPIO-enhanced MRI, contrast agents, acute heart rejection, spectral graph theory, Cheeger constant, graph cut, graph Laplacian, classification, classifier.

This work was supported by National Institute of Health grants R01EB/AI-00318 and P41EB001977.

H. H. Chang and J. M. F. Moura are with the Department of Electrical and Computer Engineering, Carnegie Mellon University, 5000 Forbes Ave., Pittsburgh, PA 15213, USA (email: hsunhsc@ece.cmu.edu; moura@ece.cmu.edu).

Y. L. Wu and C. Ho are with the Department of Biological Sciences and the Pittsburgh NMR Center for Biomedical Research, Carnegie Mellon University, Mellon Institute, 4400 Fifth Ave., Pittsburgh, PA 15213, USA.

I. INTRODUCTION

Heart failure is a major public health crisis in the United States. It is the leading cause of death and hospitalization in this country. For many patients with end-stage heart failure, heart transplantation may be the only viable treatment option. Physicians typically assess for cardiac rejection by performing frequent endomyocardial biopsies. Using biopsy samples, cardiologists monitor immune cell infiltration and other pathological characteristics of rejection. However, biopsies are invasive procedures that are subject to patient risk. In addition, due to limited sampling, biopsies may not detect focal areas of rejection.

Cellular magnetic resonance imaging (MRI) is a useful tool to non-invasively monitor the migration and localization of cells in the whole heart *in vivo* [1]. This imaging modality relies on extrinsic contrast agents, such as ultrasmall superparamagnetic iron oxide (USPIO) particles. The superior relaxivity of USPIO particles reduces signal emission in T_2^*-weighted MRI [2]. In other words, the signal attenuation created in T_2^*-weighted MR images localizes the cells containing a significant number of USPIO particles.

Mammalian cells can be labeled with MRI contrast agents either *ex vivo* or *in vivo*. In the *ex vivo* method, specific types of cells are isolated, labeled with contrast agents in culture, and then reintroduced. *In vivo* method, contrast agents are administered intravenously. *In vivo* labeling is effective for cells that can phagocytose or endocytose the contrast agents, and can be conveniently applied in the clinical studies. We adopt *in vivo* labeling in this study.

After USPIO particles are administered, circulating macrophages can endocytose USPIO particles and become USPIO-labeled macrophages. When rejection occurs, the labeled macrophages migrate to the rejecting tissue. Imaging the transplant by T_2^*-weighted MRI, dark pixels represent the infiltration of macrophages labeled by USPIO particles and identify the rejecting sites [3], [4]. For example, Figure 1 shows the left ventricular image of a rejecting cardiac allograft, where the darker signal intensities in the myocardium reveal the presence of USPIO-labeled cells, leading to the detection of the macrophage accumulation. To identify such regions, the first task is to classify the USPIO-labeled dark pixels in the image.

The usual method to classify USPIO-labeled pixels is manual classification [4]–[7], or simple thresholding of the image. Manual classification requires cardiologists to scrutinize the entire image to determine the location of the USPIO-labeled pixels. Manual classification is labor-

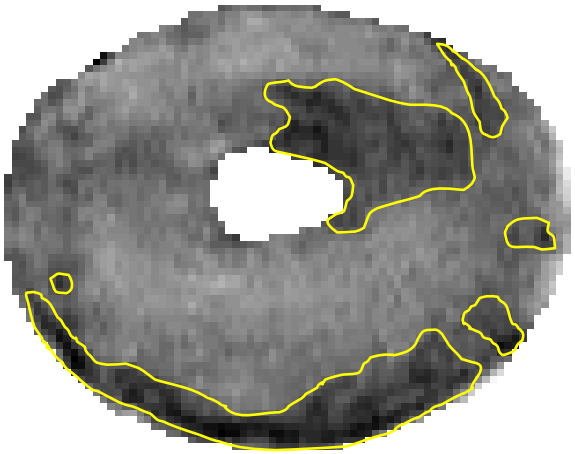

Fig. 1. A USPIO-enhanced cardiac MR image where the dark pixels are segmented. The dark pixels correspond to the locations of USPIO-labeled abnormal cells.

intensive and operator dependent. In addition, the noise introduced during the imaging, the blur induced by cardiac motion, and the partial volume effect make dark and bright pixels difficult to distinguish. Thresholding the intensities is the simplest algorithm to classify USPIO-labeled pixels; however, this method cannot handle noise. Another drawback of thresholding is that the operator has to adjust the threshold values, which may introduce inconsistent recordings. To reduce the labor involved with manual classification, to make the process robust to noise, and to achieve consistent results, we propose to develop an automatic algorithm for classification of USPIO-labeled pixels.

To design an automatic classification algorithm, we face the following challenges:

1) Macrophages accumulate in multiple regions without known pattern. For example, Figure 1 displays a rejecting heart where the boundaries of macrophage accumulation are manually determined. We can see that the macrophage spread randomly throughout the myocardium. Since there is no model describing how macrophages infiltrate, the algorithm will rely solely on the MRI data.
2) Due to noise and cardiac motion, the boundaries between the dark and bright pixels are diffuse and hard to distinguish; as such, any classification algorithm has to be robust to noise.
3) There are a large number of pixels in the myocardium. For instance, the heart shown in Figure 1 has more than 2500 myocardial pixels. This means that we have to classify more

than 2500 pixels, which may involve estimating a large number of parameters. To avoid estimating too many parameters and design the classification algorithm in a tractable way, we transform the problem into another one that expresses the classifier in terms of a small number of parameters.

4) There are two types of classifiers for our design: supervised and unsupervised. Supervised classifiers need human operators to label a subset of the pixels. The classifiers then automatically propagate the human labels to the remaining pixels. However, the human knowledge might be unreliable, so the classification results are sensitive to operators. To avoid the classification inconsistency related to operator dependence, the classifier will be unsupervised.

A. Overview of Our Approach

We formulate the task of classifying USPIO-labeled regions as a problem of graph partitioning [8]. Given a heart image, the first step is to represent the myocardium as a graph. We treat all the myocardial pixels as the vertices of a graph, and prescribe a way to assign edges connecting the vertices. Graph partitioning is a method that separates the graph into disconnected subgraphs, for example, one representing the classified USPIO-labeled region and the other representing the unlabeled region of the myocardium. The goal in graph partitioning is to find a small as possible subset of edges whose removal will separate out a large as possible subset of vertices. In graph theory terminology, the subset of edges that disjoins the graph is called a *cut*, and the measure to compare partitioned subsets of vertices is the *volume*. Graph partitioning finds the *minimal* ratio of the cut to the volume, which is called the *isoperimetric number* and is also known as the *Cheeger constant* [9] of the graph. Evaluating the Cheeger constant will determine the optimal edge cut.

The determination of the Cheeger constant, and hence of the optimal edge cut, is a combinatorial problem. We can enumerate all the possible combinations of two subgraphs partitioning the original graph, and then choose the combination with the smallest cut-to-volume ratio. However, when the number of vertices is very large, the enumeration approach is infeasible. To circumvent this obstacle, we adopt an optimization framework. We introduce a classifier, or a classification function, that determines to which class each pixel belongs, and derive from the Cheeger constant an objective functional to be minimized with respect to the classifier. The minimization leads to

the optimal classification.

If there is a complete set of basis functions on the graph, we can represent the classifier by a linear combination of the basis. There are various ways to obtain the basis functions, e.g., using the Laplacian operator [10], the diffusion kernel [11], or the Hessian eigenmap [12]. Among these, we choose the Laplacian. The spectrum of the Laplacian operator has been used to obtain upper and lower bounds on the Cheeger constant [8]; we utilize these bounds to derive our objective functional. The eigenfunctions of the Laplacian form a basis of the Hilbert space of square integrable functions defined on the graph. Thus, we express the classifier as a linear combination of the Laplacian eigenfunctions. Since the basis is known, the optimal classifier is determined by the linear coefficients in the combination. The classifier can be further approximated as a linear combination of only the *most relevant* basis functions. The approximation reduces significantly the problem of looking for a large number of coefficients to estimating only a few of them. Once we determine the optimal coefficients, the optimal classifier automatically partitions the myocardial image into USPIO-labeled and unlabeled parts.

B. Paper Organization

This paper extends our work briefly presented in [13]. The organization of this paper is as follows. Section II describes how we represent a heart image by a graph and introduces the Cheeger constant for graph partitioning. Section III details the optimal classification algorithm in the framework of spectral graph theory. In Section IV, we describe the algorithm implementation and show our experimental results for USPIO-enhanced MRI data on heart transplants. We contrast the proposed method with the results of manual classification, thresholding, another graph based algorithm, and the level set approach. Finally, Section V concludes this paper.

II. Graph Representation and Graph Partitioning

For a given USPIO-enhanced MR image, we first segment the left ventricle and remove artifacts. Then, the myocardial pixels are arranged into a single column vector indexed by a set of integers $I = \{1, 2, \cdots, N_{\text{myo}}\}$, where N_{myo} is the number of myocardial pixels. The image intensity becomes a function $f : I \mapsto \mathbb{R}$. We next describe how to represent the image as a graph.

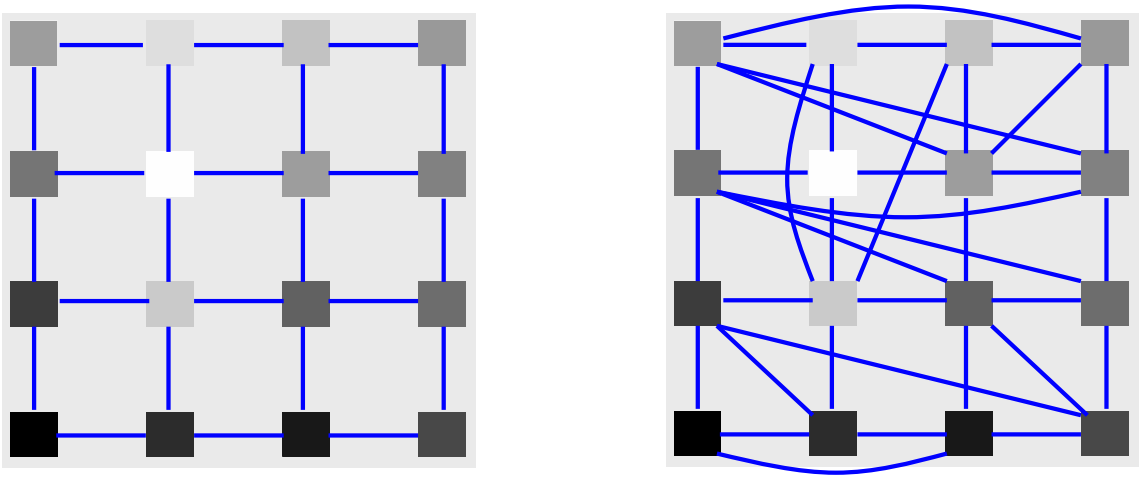

(a) Edge assignment according to the geographical neighbors.

(b) The graph representation using both geographical neighbors and feature similarities.

Fig. 2. Illustration of the graph representation of a 4×4 image.

A. Weighted Graph Representation

A graph $G(V, E)$ has a set V of vertices and a set E of edges linking the vertices. For the segmented myocardium, we treat each myocardial pixel i as a vertex v_i. We next assign edges connecting the vertices. In the graph representation, the vertices with high possibility of being drawn from the same class are linked together. There are two strategies to assign edges:

(i) Connect vertices to geographically neighboring vertices [14], because the neighborhood is usually drawn from the same class.

(ii) Connect vertices with similar features [10], because pixels in the same class generate the same features up to noise.

We adopt both strategies to build up our graph representation of the image.

With reference to Figure 2(a), consider vertex v_i corresponding to pixel i at coordinate (x_i, y_i). We connect v_i to its four neighboring vertices at coordinates $(x_i + 1, y_i)$, $(x_i - 1, y_i)$, $(x_i, y_i + 1)$, and $(x_i, y_i - 1)$. Figure 2(a) illustrates the graph representation resulting from this rule of geographical neighborhood for a 4×4 image. In this figure, each square is a pixel, and hence a vertex, and each line is an edge.

To account for strategy (ii), we need features associated with the vertices and need a metric to determine the similarity between pairs of features. To take into account noise, we treat each

pixel as a random variable and adopt the *Mahalanobis distance*, [15], as similarity measure. We stack a $N_{\text{w}} \times N_{\text{w}}$ block of pixels centered at pixel i into a column vector $\mathbf{x}_i$, which we treat as the feature vector for the vertex v_i. The Mahalanobis distance ρ_{ij} between the features $\mathbf{x}_i$, $\mathbf{x}_j$ of vertices v_i, v_j is, see [15],

$$\rho_{ij} = \sqrt{(\mathbf{x}_i - \mathbf{x}_j)^T \Sigma_{i,j}^{-1} (\mathbf{x}_i - \mathbf{x}_j)}\,, \tag{1}$$

where $\Sigma_{i,j}$ is the covariance matrix between $\mathbf{x}_i$ and $\mathbf{x}_j$. When the distance ρ_{ij} is below a predetermined threshold τ_ρ, the vertices v_i, v_j are connected by an edge; otherwise, they are disconnected. Figure 2(b) shows the final graph representation of the 4×4 image example using both geographical neighbors and feature similarities.

In graph theory, we usually consider *weighted* graphs [8]. Since not all connected pairs of vertices have the same distances, we capture this fact by using a weight function on the edges. We adopt a Gaussian kernel, suggested by Belkin and Niyogi [10] and used also by Coifman *et al.* [11], to compute the weights W_{ij} on edges e_{ij} connecting vertices v_i and v_j:

$$W_{ij} = \begin{cases} \exp\left(-\frac{\rho_{ij}^2}{\sigma^2}\right), & \text{if there is edge } e_{ij} \\ 0\,, & \text{if no edge } e_{ij} \end{cases}, \tag{2}$$

where σ is the Gaussian kernel parameter. The larger σ is, the more weight far-away vertices will exert on the weighted graph. The weight W_{ij} is large when the features of two linked vertices v_i, v_j are similar.

The weighted graph is equivalently represented by its $N_{\text{myo}} \times N_{\text{myo}}$ *weighted adjacency matrix* $\mathbf{W}$ whose elements W_{ij} are the edge weights in equation (2). Note that the matrix $\mathbf{W}$ has a zero diagonal because we do not allow the vertices to be self-connected; it is symmetric since $W_{ij} = W_{ji}$.

B. Graph Partitioning and the Cheeger Constant

Classification is to partition the set of pixels into disjoint sets. In graph terms, we divide the graph $G(V, E)$ into two subgraphs. The task is to find out a subset E_0 of edges, called an *edge cut* such that removing this cut separates the graph $G(V, E)$ into two disconnected subgraphs $G_1 = (V_1, E_1)$ and $G_2 = (V_2, E_2)$, where $V = V_1 \cup V_2$, $\emptyset = V_1 \cap V_2$, and $E = E_0 \cup E_1 \cup E_2$. Taking the example of the 4×4 image again, the dotted edges shown in Figure 3(a) assemble an edge

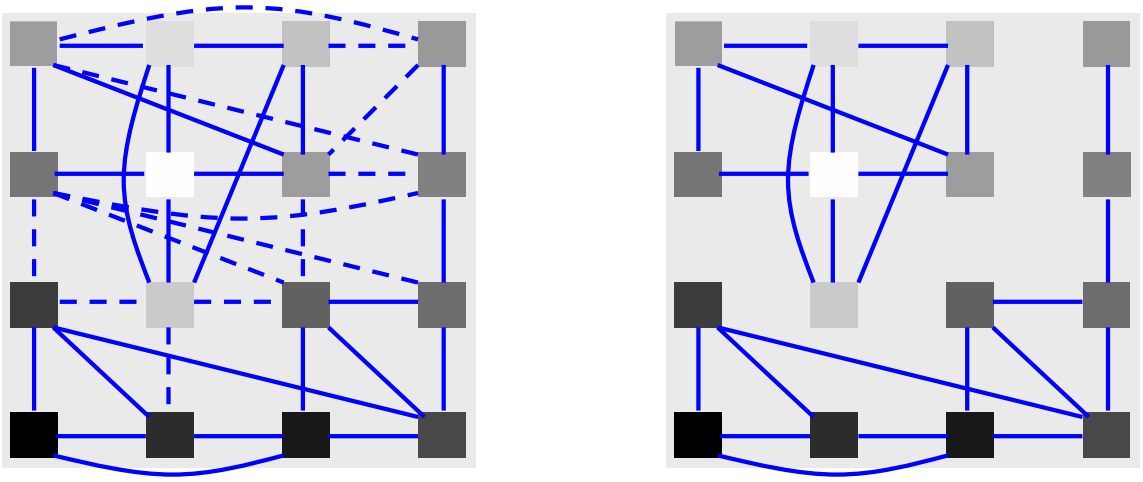

(a) Dotted edges assemble an edge cut. (b) Removal of the edge cut partitions the graph.

Fig. 3. Conceptualization of an edge cut associated to the 4×4 image in Figure 2(b).

cut for the graph. The removal of this edge cut partitions the graph into two parts as shown in Figure 3(b).

In the framework of spectral graph theory [8], we define an *optimal* edge cut by looking for the Cheeger constant $\Gamma(V_1)$ of the graph,

$$\Gamma(V_1) = \min_{V_1 \subset V} \frac{|E_0(V_1, V_2)|}{\text{vol}(V_1)} , \tag{3}$$

assuming that $\text{vol}(V_1) \leq \text{vol}(V_2)$. In equation (3), $|E_0(V_1, V_2)|$ is the sum of the edge weights in the cut E_0:

$$|E_0(V_1, V_2)| = \sum_{v_i \in V_1, v_j \in V_2} W_{ij} . \tag{4}$$

The volume $\text{vol}(V_1)$ of V_1 is defined as the sum of the vertex degrees in V_1:

$$\text{vol}(V_1) = \sum_{v_i \in V_1} d_i , \tag{5}$$

where the degree d_i of the vertex v_i is defined as

$$d_i = \sum_{v_j \in V} W_{ij} . \tag{6}$$

To denote the partition of the graph vertices, we introduce an indicator vector χ for V_1 whose elements are defined as

$$\chi_i = \begin{cases} 1, & \text{if } v_i \in V_1 \\ 0, & \text{if } v_i \in V_2 \end{cases} . \tag{7}$$

In Appendix I, we derive the Cheeger constant in terms of the indicator vector χ:

$$\Gamma(\chi) = \min_{\chi} \frac{\chi^T \mathbf{L} \chi}{\chi^T \mathbf{d}} \,, \tag{8}$$

where $\mathbf{L}$ is the graph Laplacian defined in (48) and $\mathbf{d}$ is the vector collecting vertex degrees. The optimal graph partitioning corresponds to the optimal indicator vector

$$\hat{\chi} = \arg\min_{\chi} \frac{\chi^T \mathbf{L} \chi}{\chi^T \mathbf{d}} \,. \tag{9}$$

C. Objective Functional for Cheeger Constant

In equation (8), the minimization of the cut-to-volume ratio is equivalent to minimizing an objective functional

$$Q(\chi) = \chi^T \mathbf{L} \chi - \beta \chi^T \mathbf{d} \,, \tag{10}$$

where β is the weight. The objective $Q(\chi)$ is convex, because the graph Laplacian $\mathbf{L}$ is positive semidefinite, see Appendix I. In addition, the second term $0 \leq \chi^T \mathbf{d} \leq \text{vol}(V)$ is finite, so the minimizer $\hat{\chi}$ exists.

Since at each vertex the indicator is either 1 or 0, see equation (7), there are $2^{N_{\text{myo}}}$ candidate indicator vectors. When the number of pixels N_{myo} in the myocardium is large, it is not computationally feasible to minimize the objective by enumerating all the candidate indicator vectors. The next section proposes a novel algorithm to avoid this combinatorial problem.

III. Optimal Classification Algorithm

This section develops the optimal classifier that utilizes the Cheeger constant.

A. Spectral Analysis of the Graph Laplacian $\mathbf{L}$

The spectral decomposition of the graph Laplacian $\mathbf{L}$, which is defined in equation (48), gives the eigenvalues $\{\lambda_n\}_{n=1}^{N_{\text{myo}}}$ and eigenfunctions $\{\phi^{(n)}\}_{n=1}^{N_{\text{myo}}}$. By convention, we index the eigenvalues in ascending order. Because the Laplacian $\mathbf{L}$ is symmetric and positive semidefinite, its spectrum $\{\lambda_n\}$ is real and nonnegative and its rank is $N_{\text{myo}} - 1$. In the framework of spectral graph theory [8], the eigenfunctions $\{\phi^{(n)}\}$ assemble a complete set and span the Hilbert space of square integrable functions on the graph. Hence, we can express any square integrable function on the graph as a linear combination of the basis functions $\{\phi^{(n)}\}$. The domain of the eigenfunctions

are vertices, so the eigenfunctions $\{\phi^{(n)}\}$ are discrete and are represented by vectors. We note that both the eigenfunctions and the vertices are indexed by the set of integers $I = \{1, 2, \cdots, N_{\text{myo}}\}$. Eigenfunction $\phi^{(n)}$ is the vector

$$\phi^{(n)} = [\phi_1^{(n)}, \phi_2^{(n)}, \cdots, \phi_{N_{\text{myo}}}^{(n)}]^T. \tag{11}$$

We list here the properties of the spectrum of the Laplacian (see see [8] for additional details) that will be utilized to develop the classification algorithm:

1) For a *connected* graph, there is only one zero eigenvalue λ_1, and the spectrum is

$$0 = \lambda_1 < \lambda_2 \leq \cdots \leq \lambda_{N_{\text{myo}}}\,. \tag{12}$$

The first eigenvector $\phi^{(1)}$ is constant, i.e.,

$$\phi^{(1)} = \alpha[1, 1, \cdots, 1]^T\,, \tag{13}$$

where $\alpha = \frac{1}{\sqrt{N_{\text{myo}}}}$ is the normalization factor for $\phi^{(1)}$.

2) The eigenvectors $\phi^{(n)}$ with nonzero eigenvalues have zero averages,

$$\sum_{i=1}^{N_{\text{myo}}} \phi_i^{(n)} = 0\,. \tag{14}$$

The low order eigenvectors correspond to low frequency harmonics.

3) For a *connected* graph, the Cheeger constant Γ defined by (8) is upper and lower bounded by the following inequality:

$$\frac{1}{2}\lambda_2 \leq \Gamma < \sqrt{2\lambda_2}\,. \tag{15}$$

Due to the edge assignment strategy of geographical neighborhood, see Section II, our graphs representing the heart images are connected. Therefore, the spectral properties in (12) and (15) hold in our case, besides the property (14) that holds in general.

B. Expression of Classifier

We now consider the graph $G(V, E)$ that describes the myocardium in an MRI heart image. The classifier $\mathbf{c}$ partitioning the graph vertex set V into two classes V_1 and V_2 is defined as

$$c_i = \begin{cases} 1, & \text{if } v_i \in V_1 \\ -1, & \text{if } v_i \in V_2 \end{cases}. \tag{16}$$

Utilizing the spectral graph analysis, we express the classifier in terms of the eigen-basis $\{\phi^{(n)}\}$

$$\mathbf{c} = \sum_{n=1}^{N_{\text{myo}}} a_n \phi^{(n)} = \Phi \mathbf{a} \,, \tag{17}$$

where a_n are the coordinates of the eigen representation, $\mathbf{a} = [a_1, a_2, \cdots, a_{N_{\text{myo}}}]^T$ is a vector stacking the coefficients, and Φ is a matrix collecting the eigen-basis

$$\Phi = \left[\phi^{(1)}, \phi^{(2)}, \cdots, \phi^{(N_{\text{myo}})}\right] \,. \tag{18}$$

The design of the optimal classifier $\mathbf{c}$ becomes now the problem of estimating the linear combination coefficients a_n.

C. Objective Functional for Classification

In equation (8), the Cheeger constant is expressed in terms of the set indicator vector χ that takes 0 or 1 values. On the other hand, the classifier $\mathbf{c}$ defined in (16) takes ± 1 values. We relate χ and $\mathbf{c}$ by the standard Heaviside function $\mathcal{H}(x)$ defined by

$$\mathcal{H}(x) = \begin{cases} 1, & \text{if } x \geq 0 \\ 0, & \text{if } x < 0 \end{cases} \,. \tag{19}$$

Hence, the indicator vector $\chi = [\chi_1, \chi_2, \cdots, \chi_{N_{\text{myo}}}]^T$ for the set V_1 is given by

$$\chi_i = \mathcal{H}(c_i) \,. \tag{20}$$

In equation (20), the indicator χ is a function of the classifier $\mathbf{c}$ using the Heaviside function $\mathcal{H}$. Furthermore, by (17), the classifier $\mathbf{c}$ is parametrized by the coefficient vector $\mathbf{a}$, so the objective functional Q is parametrized by this vector $\mathbf{a}$, i.e.,

$$Q(\mathbf{a}) = \chi(\mathbf{c}(\mathbf{a}))^T \mathbf{L} \chi(\mathbf{c}(\mathbf{a})) - \beta \chi(\mathbf{c}(\mathbf{a}))^T \mathbf{d} \,. \tag{21}$$

Minimizing Q with respect to $\mathbf{a}$ gives the optimal coefficient vector $\hat{\mathbf{a}}$, which leads to the optimal classifier $\mathbf{c} = \Phi \hat{\mathbf{a}}$. Using eigen-basis to represent the classifier transforms the problem of the combinatorial optimization in (10) to estimating the real-valued coefficient vector $\mathbf{a}$ in (21).

To avoid estimating too many parameters, we relax the classification function to a smooth function, which simply requires the first p harmonics in its expression in terms of the eigen-basis. The classifier $\mathbf{c}$ is now

$$\mathbf{c} = \sum_{n=1}^{p} a_n \phi^{(n)} = \Phi \mathbf{a} \,, \tag{22}$$

where $\mathbf{a} = [a_1, a_2, \cdots, a_p]^T$ and $\Phi = \left[\phi^{(1)}, \phi^{(2)}, \cdots, \phi^{(p)}\right]$. The estimation of the N_{myo} parameters in (17) is reduced to the $p \ll N_{\text{myo}}$ parameters in (22). As long as p is chosen small enough, the latter is more numerically tractable than the former.

Another concern in the objective functional (10) is the weighting parameter β. If we knew the Cheeger constant Γ, we could set $\beta = \Gamma$ and the objective function would be

$$Q(\chi) = \chi^T \mathbf{L}\chi - \Gamma \chi^T \mathbf{d}\,. \tag{23}$$

The solution would correspond to $Q(\chi) = 0$, see (8). However, we cannot set $\beta = \Gamma$ beforehand, since the Cheeger constant $\Gamma(\hat{\chi})$ is dependent on the unknown optimal indicator vector $\hat{\chi}$.

We can reasonably predetermine β by using one of the spectral properties of the graph Laplacian: The upper and lower bounds of the Cheeger constant are related to the first nonzero eigenvalue λ_2 of the graph Laplacian, see equation (15). The bounds restrain the range of values for the weight β. For simplicity, we set β to the average of the Cheeger constant's upper and lower bounds,

$$\beta = \frac{1}{2}\left(\frac{1}{2}\lambda_2 + \sqrt{2\lambda_2}\right)\,. \tag{24}$$

D. Minimization Algorithm

Taking the gradient of $Q(\mathbf{a})$, we obtain

$$\frac{\partial Q}{\partial \mathbf{a}} = 2\left(\frac{\partial \chi^T}{\partial \mathbf{a}}\right)\mathbf{L}\chi - \beta\left(\frac{\partial \chi^T}{\partial \mathbf{a}}\right)\mathbf{d}\,. \tag{25}$$

In equation (25), the computation of $\left(\frac{\partial \chi^T}{\partial \mathbf{a}}\right)$ is

$$\left(\frac{\partial \chi^T}{\partial \mathbf{a}}\right) = \left[\frac{\partial \chi_1}{\partial \mathbf{a}}, \frac{\partial \chi_2}{\partial \mathbf{a}}, \cdots, \frac{\partial \chi_{N_{\text{myo}}}}{\partial \mathbf{a}}\right] \tag{26}$$

$$= \begin{bmatrix} \frac{\partial \chi_1}{\partial a_1} & \frac{\partial \chi_2}{\partial a_1} & \cdots & \frac{\partial \chi_{N_{\text{myo}}}}{\partial a_1} \\ \vdots & \vdots & \cdots & \vdots \\ \frac{\partial \chi_1}{\partial a_p} & \frac{\partial \chi_2}{\partial a_p} & \cdots & \frac{\partial \chi_{N_{\text{myo}}}}{\partial a_p} \end{bmatrix}\,. \tag{27}$$

Using the chain rule, the entries $\left(\frac{\partial \chi^T}{\partial \mathbf{a}}\right)_{mn}$ are

$$\left(\frac{\partial \chi^T}{\partial \mathbf{a}}\right)_{mn} = \frac{\partial \chi_n}{\partial a_m} \tag{28}$$

$$= \frac{\partial \chi_n}{\partial c_n}\frac{\partial c_n}{\partial a_m} \tag{29}$$

$$= \delta(c_n)\frac{\partial \sum_{j=1}^{p} a_j \phi_n^{(j)}}{\partial a_m} \tag{30}$$

$$= \delta(c_n)\phi_n^{(m)} \,. \tag{31}$$

In (30), $\delta(x)$ is the delta (generalized) function defined as the derivative of the Heaviside function $\mathcal{H}(x)$.

To facilitate numerical implementation, we use the regularized Heaviside function $\mathcal{H}_\epsilon$ and the regularized delta function δ_ϵ; they are defined, respectively, as

$$\mathcal{H}_\epsilon(x) = \frac{1}{2}\left[1 + \frac{2}{\pi}\arctan\left(\frac{x}{\epsilon}\right)\right] \,, \tag{32}$$

and

$$\delta_\epsilon(x) = \frac{d\mathcal{H}_\epsilon(x)}{dx} = \frac{1}{\pi}\left(\frac{\epsilon}{\epsilon^2 + x^2}\right) \,. \tag{33}$$

Replaced with the regularized delta function, the explicit expression of $\left(\frac{\partial \chi^T}{\partial \mathbf{a}}\right)$ is

$$\left(\frac{\partial \chi^T}{\partial \mathbf{a}}\right) = \begin{bmatrix} \delta_\epsilon(c_1)\phi_1^{(1)} & \delta_\epsilon(c_2)\phi_2^{(1)} & \cdots & \delta_\epsilon(c_{N\text{myo}})\phi_{N\text{myo}}^{(1)} \\ \vdots & \vdots & \cdots & \vdots \\ \delta_\epsilon(c_1)\phi_1^{(p)} & \delta_\epsilon(c_2)\phi_2^{(p)} & \cdots & \delta_\epsilon(c_{N\text{myo}})\phi_{N\text{myo}}^{(p)} \end{bmatrix} \tag{34}$$

$$= \Phi^T \Delta \,, \tag{35}$$

where we define

$$\Delta = \text{diag}\left(\delta_\epsilon(c_1), \delta_\epsilon(c_2), \cdots, \delta_\epsilon(c_{N\text{myo}})\right) \,. \tag{36}$$

Substituting (35) into (25), the gradient of the objective has the compact form

$$\frac{\partial Q}{\partial \mathbf{a}} = 2\Phi^T \Delta \mathbf{L} \chi - \beta \Phi^T \Delta \mathbf{d} \,. \tag{37}$$

The optimal coefficient vector $\hat{\mathbf{a}}$ is obtained by looking for $\frac{\partial Q}{\partial \mathbf{a}} = 0$. We have to solve the minimization numerically, because the unknown $\mathbf{a}$ is inside the matrix Δ and the vector χ. We

adopt the gradient descent algorithm to iteratively find the solution $\hat{\mathbf{a}}$. The classifier $\mathbf{c}$ is then determined by

$$\mathbf{c} = \Phi\hat{\mathbf{a}}\,. \tag{38}$$

The vertices with indicators $\chi_i = \mathcal{H}(c_i) = 1$ correspond to class V_1 and 0 correspond to class V_2. To select the desired USPIO-labeled regions, the operator simply chooses one of the two classes.

E. Algorithm Summary

There are two major algorithms in the classifier development: graph representation and classification. We summarize them in the Algorithms 1 and 2, respectively.

Algorithm 1 The graph representation algorithm

procedure GRAPHREP(f) ▷ Load the image f
  Segment the left ventricle
  Index all the myocardial pixels by a set of integers $I = \{1, \cdots, N_{\text{myo}}\}$
  Initialize $\mathbf{W}$ as an $N_{\text{myo}} \times N_{\text{myo}}$ zero matrix
  for all $i \neq j \in I$ **do**
    Compute Mahalanobis distance ρ_{ij} by (1)
    if $\rho_{ij} < \tau_\rho$ or i, j are geographical neighbors **then**
      $W_{ij} \leftarrow$ Compute edge weight W_{ij} by (2)
    end if
  end for
  return $\mathbf{W}$
end procedure

IV. EXPERIMENTS

This section presents the performance of the classifier with experimentally obtained USPIO-enhanced MRI of phantoms and of transplanted rat hearts. We implement our algorithm with MATLAB® on a computer with a 3 GHz CPU and 1 GB RAM. After data acquisition, we normalize the heart image intensities to range from 0 to 1 and manually segment the left ventricle.

Algorithm 2 The classification algorithm

procedure CLASSIFIER($\mathbf{W}$)
  Compute graph Laplacian $\mathbf{L}$ by (48)
  Eigendecompose $\mathbf{L}$ to obtain $\{\lambda_n\}$ and $\{\phi^{(n)}\}$
  Compute coefficient β by (24)
  Initialize classifier coefficient $\mathbf{a} = \mathbf{1}$ and objective $Q = \infty$
  repeat
    $\mathbf{c} \leftarrow$ Compute classifier $\mathbf{c}$ by (22)
    $\chi \leftarrow$ Compute indicator vector χ by (20)
    $Q \leftarrow$ Compute objective Q by (21)
    $\mathbf{a} \leftarrow$ Compute $\mathbf{a} - \frac{\partial Q}{\partial \mathbf{a}}$ by (37)
  until $\frac{\partial Q}{\partial \mathbf{a}} = 0$
  return χ
end procedure

Classifier Setting: There are several parameters needed for running the classifier; their values are described in the following.

- Each vertex v_i is associated with a $N_{\text{w}} \times N_{\text{w}}$ block of pixels centered at pixel i for computing the Mahalanobis distance, see Section II-A. We set $N_{\text{w}} = 3$. If N_{w} is 1, noise is not taken into account. If N_{w} is large, the graph takes better account of the impact of the noise but the computational time for constructing the graph increases. Our choice of N_{w} is a compromise between these two issues.
- To derive the image graph, we set $\sigma = 0.1$ when computing the edge weights in (2). This choice of σ is suggested by Shi and Malik [14], who indicate empirically that σ should be set at 10% of the range of the image intensities.
- The parameter ϵ for the regularized Heaviside and delta functions in (32) and (33), respectively, is set to 0.1. The smaller the parameter ϵ is, the sharper these two regularized functions are. For $\epsilon = 0.1$, the regularized functions are a good approximation to the standard ones.
- To determine the number p of lowest order eigenfunctions used to represent the classifier $\mathbf{c}$, we tested values of p from 5 to 20. We obtain the best results for $p = 16$.

- To reach the minimum of the objective functional, we solve $\frac{\partial Q}{\partial \mathbf{a}} = 0$ recursively. We stop the iterative process when the norm of the gradient is smaller than 10^{-4} or when the minimization reaches 200 iterations. This number of iterations led to convergence in all of our experiments, although, in most cases, we observed convergence within the first 100 iterations.

A. Phantom Study

We design a phantom to investigate how our algorithm performs under various contrast-to-noise ratios (CNRs). The phantom sample consists of three tubes that contain different concentration of iron-oxide particles and that are surrounded by water. We imaged the phantom with a Bruker AVANCE DRX 4.7-Tesla system with a 5.5-cm home-built surface coil. To generate CNRs from low to high, we run three series of scans:

- Series 1: fixed repetition time (TR) = 1000 ms and number of signal averages (NEX) = 2; varied echo time (TE) = 3 to 15 ms.
- Series 2: fixed TR = 500 ms and TE = 5 ms; varied NEX = 1 to 12.
- Series 3: fixed TE = 5 ms and NEX = 2; varied TR = 300 to 1500 ms.

To compute CNR of an image, we begin with calculating signal-to-noise ratios (SNRs) of USPIO-labeled and -unlabeled regions:

$$\text{SNR}_{\text{lab}} = \frac{\text{average signal of USPIO-labeled regions}}{\text{standard deviation of background noise}}, \tag{39}$$

$$\text{SNR}_{\text{unlab}} = \frac{\text{average signal of unlabeled regions}}{\text{standard deviation of background noise}}. \tag{40}$$

Then, CNR is determined as

$$\text{CNR} = \left|\text{SNR}_{\text{lab}} - \text{SNR}_{\text{unlab}}\right|. \tag{41}$$

The percentage of misclassified pixels is the criterion to evaluate the performance of the classifier. Figure 4 plots the percentage error versus CNR for the three series of scans. With reference to Figures 4(a), 4(b) and 4(c), the proposed algorithm achieves perfect classification when the CNR is larger than 6, but the error increases considerably when the CNR is below 5. This phantom study suggests that the MRI protocol should be designed to reach CNR = 6 or above so that the classifier can perform without errors.

TABLE I

SNR AND CNR VERSUS POD.

	POD3	POD4	POD5	POD6	POD7
SNR of USPIO-unlabeled myocardium	24.87	20.79	16.77	25.36	21.71
SNR of USPIO-labeled myocardium	12.89	13.11	9.71	11.81	10.38
CNR of USPIO-enhanced myocardium	11.98	7.68	7.06	13.55	11.33

B. Cardiac Rejection Study

USPIO-Enhanced MRI of Heart Transplants: We have studied the acute cardiac rejection of transplanted hearts using our heterotopic working rat heart model. All rats were male inbred Brown Norway (BN; RT1n) and Dark Agouti (DA; RT1a), obtained from Harlan (Indianapolis, IN), with body weight between 0.18 and 0.23 kg each. We transplanted DA hearts to BN hosts. Home-made dextran-coated USPIO particles [3] of 27 nm in size were administered intravenously one day prior to MRI with a dosage of 4.5 mg per kg bodyweight.

To investigate the acute cardiac progression, we have imaged five different transplanted rat hearts on post-operation days (PODs) 3, 4, 5, 6, and 7, individually. In our heterotopic rat cardiac transplant model, mild acute rejection begins on POD 3, progresses to moderate rejection on PODs 4 and 5, severe and very severe rejection on PODs 6 and 7, respectively [4]. Each heart was imaged with ten short-axis slices covering the entire left ventricle. *In vivo* imaging was carried out on the same machine in the phantom study. T_2^*-weighted imaging was acquired with gradient echo recall sequence. Respiratory as well as electrocardiogram gating is used to control respiratory and heart motion artifacts for MR imaging. The MRI protocol has the following parameters: TR = one cardiac cycle (about 180 ms); TE = 8 to 10 ms; NEX = 4; flip angle = $90°$; field of view = 3 to 4 cm; slice thickness = 1 to 1.5 mm; in-plane resolution = 117 to 156 μm. The MRI protocol is optimized to guarantee that the classifier works in a valid CNR range. Table I summarizes the SNRs and CNRs in various POD data. The CNRs are all greater than 6, which was the threshold for the classifier to achieve perfect classification in the phantom study.

Automatic Classification Results: Figure 5(a) shows different transplanted hearts imaged on PODs 3, 4, 5, 6, and 7. Each image is the sixth slice out of ten acquired slices for the

heart; its location in the heart corresponds to the equator of the left ventricle. Then, we apply our classification algorithm to the images. Figure 5(b) shows the detected USPIO-labeled areas denoted by red (darker pixels). Unlike time-consuming manual classification, our algorithm takes less than three minutes to determine the regional macrophage accumulation for each image.

To take into account the 3D heart, we process slices 3 to 8 out of 10 for the current study. We do not use the first two and the last two slices because they do not clearly contain the myocardium. The classifier automatically determines slice by slice the USPIO-labeled regions of the heart.

Validation with Manual Classification: Wu *et al.* [4] have shown that the dark patches in the MR images are due to those macrophages labeled with USPIO particles whose presence is correlated histologically and immunologically with acute cardiac rejection. Since the best validation option right now is to compare with classification results by a human expert, we treat manually determined USPIO-labeled pixels as the gold standard. In our data set, we can see that manual classification of the heart slices is appropriate for all PODs, except POD5, as we will discuss shortly. Manual classification of all the heart slices at all PODs has been carried out before running the automatic classification. Figure 5(c) shows the manually classified USPIO-labeled regions. Our automatically detected regions show good agreement with the manual results in all slices and PODs, except for POD5. This qualitative validation suggests that our automatic approach is useful in the study of heart rejection based on USPIO-enhanced MRI data.

To quantitatively evaluate the quality of the automatic classification, we have compared the total area of USPIO-labeled regions determined by the classifier and determined manually. In Figure 6(a), we plot the total macrophage accumulation percentage for slice 6 as a function of the PODs for the data used in Figure 5. Figure 6(b) shows similar results but for the whole 3D heart.

To appreciate better how much the classifier deviates from manual classification, we define the percentage error as

$$P(\varepsilon) = \frac{|(\text{automatic USPIO-labeled area}) - (\text{manual USPIO-labeled area})|}{\text{myocardium area}}\,, \qquad (42)$$

which we show in Figure 7(a). Since the noise levels in different slices are not identical, the classification errors vary from slice to slice. The deviation of the classifier, usually below 4%, shows the very good agreement between the classifier and manual classification for all PODs,

except POD5.

We now consider the discrepancy between the automatic classifier and the manual classification results in POD5. The five slices in POD5 heart have percentage errors larger than 6%, with one of them exceeding 10%. POD5 data sets are the most challenging among all POD data sets. This is because POD5 slices are the most noisy, see Table I, and where the macrophages spread dispersively, as rejection spreads from the periphery of the heart (epicardium) to the whole heart. With reference to the POD5 image (middle image on the left column) in Figure 5(a), we see many dark punctate blobs corresponding to the presence of macrophages. Manual selection of these blobs is challenging to a human operator. By missing many of these, the lines displaying the manual classification results (percentage area or percentage volume) in Figures 6(a) and 6(b), respectively, fail to be nondecreasing, showing a dip at POD5. Were this true, the level of rejection would have decreased from POD4 to POD5, clearly a contradiction, since the animal models were not treated and rejection becomes more prevalent as time progresses. In contrast, the corresponding plot lines for the classifier are monotonic—while they track well the manual classification results everywhere else, they deviate from the dip at POD5.

Comparisons with Other Classification Approaches: In addition to manual classification, simple thresholding is the common automatic method used for classification of USPIO-labeled regions. Figure 8(a) shows the classification results obtained by thresholding the images in Figure 5(a). Figures 6(a) and 6(b) also plot the macrophage accumulation curves using thresholding. The error analysis of the thresholding classification is shown in Figure 7(b) using the same definition for percentage deviation in (42). Although the classification results by our classifier and by thresholding shown in Figures 5(b) and 8(a), respectively, are visually indistinguishable, the quantitative error analysis shown in Figure 7(b) demonstrates that the thresholding method has higher error rates in most slices than automatic classifier. Further, thresholding is not robust, with error rates that can range from 0.5% to 18.5%, usually with error rates larger than 6%. Thresholding is prone to inconsistency because of the subjectivity in choosing the thresholds and because it does not account for the noise and motion blurring the images.

We provide another comparison by contrasting our algorithm with an alternative classifier, namely, the *isoperimetric partitioning* algorithm proposed by Grady and Schwartz [16]. The isoperimetric algorithm uses also a graph representation, which includes a geographical neighborhood only, not taking into account the noise for edge weights, as in our approach. The

isoperimetric algorithm tries to minimize the objective function $\mathbf{c}^T\mathbf{L}\mathbf{c}$, where $\mathbf{c}$ is the real-valued classification function and $\mathbf{L}$ is the graph Laplacian. The minimization is equivalent to solving the linear system $\mathbf{L}\mathbf{c} = \mathbf{0}$. We applied this method to the images in Figure 5(a). The classification results are shown in Figure 8(b). Comparing these results with the manual classification results in Figure 5(c), we conclude that the isoperimetric partitioning algorithm fails completely on this data set. The problems with this method are twofold. First, the objective function captures the edge cut but ignores the volume enclosed by the edge cut. This contrasts with our functional, the Cheeger constant, that captures faithfully the goal of minimizing the cut-to-volume ratio. Second, although the desired classifier of the isoperimetric partitioning is a binary function, the actual classifier it considers is a relaxed real-valued function. Our approach addresses this issue via the Heaviside function.

The final comparison is between our proposed method and the *level set* approach [17], [18], which has been applied successfully to segment the heart stuctures [19]. The level set method finds automatically contours that are the zero level of a level set function defined on the image and that are boundaries between USPIO-labeled and -unlabeled pixels. The optimal level set is obtained to meet the desired requirements: (i) the regions inside and outside the contours have distinct statistical models, (ii) the contours capture sharp edges, and (iii) the contours are as smooth as possible. Finally, we can classify the pixels enclosed by the optimal contours as USPIO-labeled areas. The experimental results using the level set approach are shown in Figures 7(c) and 8(c). In the heart images, macrophages are present not only in large regions but also in small blobs with irregular shapes whose edges do not provide strong forces to attract contours. The contour evolution tends to pass small blobs and capture large continua, leading to more misclassification than our proposed method.

The performance of our proposed classifier may be affected when artifacts are present in the MR images. Our method establishes the graphical representation of the images from geographical and intensity similarities among pixels. If a myocardial region has hypointensity due to artifacts, its intensity features are similar to those of USPIO-labeled pixels and the classifier will have a hard time to distinguish correctly between the artifacts and the USPIO-labeled regions. Although artifacts were not present in our data sets, the operator may need to invoke an artifact removal algorithm before running our classifier.

The classifier presented in this paper performs binary classification of the myocardial pixels

and then determines the rejection severity by counting the number of pixels per volume involved in USPIO-labeling. Since macrophage infiltration depends on the rejection severity, less for mild rejection, more for severe rejection, the USPIO-labeled rejecting tissue does not contribute the same levels of MR signals. In future work, we will extend this classifier to handle multiple classes to provide an integrated mechanism to measure rejection severity.

V. Conclusions

This paper develops an automatic algorithm to classify regional macrophage accumulation of allografts imaged by USPIO-enhanced MRI. Automatic classification is desirable. It lightens the manual work of an expert, prevents inconsistencies resulting from different choices of thresholds that usually plague classification by human operators, and, by accounting in its design explicitly for noise, it is robust to noise. The classifier developed in this paper can assist in studying rejection in heart transplants.

We formulate the classification task as a graph partitioning problem. We associate to an MR image a graph where the graph vertices denote pixels and the graph edges connect neighboring and similar pixels. We treat the classifier as a binary function on the graph. The eigendecomposition of the graph Laplacian provides a basis to represent the classifier. The binary classifier is relaxed to a smooth function by linearly combining several low order eigen basis functions. The optimal classifier is designed to minimize an objective functional derived from the Cheeger constant of the graph. Our experimental results with USPIO-enhanced MRI data of small animals' cardiac allografts undergoing rejection show that the Cheeger graph partitioning based classifier can determine accurately the regions of macrophage infiltration. These experiments show that it presents better performance than other methods like the commonly used thresholding, the isoperimetric algorithm, and a level set based approach.

Appendix I

Expression of the Cheeger constant Γ in terms of the indicator vector χ

We can rewrite the vertex degree d_i, see (6), by considering the vertices v_j in either V_1 or V_2; i.e.,

$$d_i = \sum_{v_j \in V_1} W_{ij} + \sum_{v_j \in V_2} W_{ij} \; . \tag{43}$$

Assuming that the vertex v_i is in V_1, the second term in equation (43) is the contribution of v_i made to the edge cut $|E_0(V_1, V_2)|$. Taking into account all the vertices in V_1, we have the edge cut

$$|E_0(V_1, V_2)| = \sum_{v_i \in V_1} \sum_{v_j \in V_2} W_{ij} \tag{44}$$

$$= \sum_{v_i \in V_1} \left(d_i - \sum_{v_j \in V_1} W_{ij} \right) . \tag{45}$$

To write equation (45) in a more compact form, we use the indicator vector χ for V_1, defined in (7). It follows that the edge cut (45) is

$$|E_0(V_1, V_2)| = \chi^T \mathbf{D} \chi - \chi^T \mathbf{W} \chi \tag{46}$$

$$= \chi^T \mathbf{L} \chi \, , \tag{47}$$

where $\mathbf{D} = \text{diag}\left(d_1, d_2, \cdots, d_{N_{\text{myo}}}\right)$ is a diagonal matrix of vertex degrees, and

$$\mathbf{L} = \mathbf{D} - \mathbf{W} \tag{48}$$

is the Laplacian of the graph, see [8]. Because $\mathbf{D}$ is diagonal and $\mathbf{W}$ is symmetric, $\mathbf{L}$ is symmetric. Further, $\mathbf{L}$ is positive semidefinite since the row sums of $\mathbf{L}$ are zeros.

Using the indicator vector χ, we express the volume $\text{vol}(V_1)$ as

$$\text{vol}(V_1) = \sum_{v_i \in V_1} d_i = \chi^T \mathbf{d} \, , \tag{49}$$

where $\mathbf{d}$ is the column vector collecting all the vertex degrees. Replacing (47) and (49) into the Cheeger constant (3), we write the Cheeger constant in terms of the indicator vector χ:

$$\Gamma(\chi) = \min_{\chi} \frac{\chi^T \mathbf{L} \chi}{\chi^T \mathbf{d}} \, . \tag{50}$$

REFERENCES

[1] C. Ho and T. K. Hitchens, "A non-invasive approach to detecting organ rejection by MRI: monitoring the accumulation of immune celss at the transplanted organ," *Current Pharmaceutical Biotechnology*, vol. 5, pp. 551–566, December 2004.

[2] R. Weissleder, G. Elizondo, J. Wittenberg, C. A. Rabito, H. H. Bengele, and L. Josephson, "Ultrasmall superparamagnetic iron oxide: Characterization of a new class of contrast agents for MR imaging," *Radiology*, vol. 175, pp. 489–493, May 1990.

[3] S. Kanno, Y. L. Wu, P. C. Lee, S. J. Dodd, M. Williams, B. P. Griffith, and C. Ho, "Macrophage accumulation associated with rat cardiac allograft rejection detected by magnetic resonance imaging with ultrasmall superparamagnetic iron oxide particles," *Circulation*, vol. 104, pp. 934–938, August 2001.

[4] Y. L. Wu, Q. Ye, L. M. Foley, T. K. Hitchens, K. Sato, J. B. Williams, and C. Ho, "*In situ* labeling of immune cells with iron oxide particles: An approach to detect organ rejection by cellular MRI," *Proceedings of the National Academy of Sciences of the United States of America*, vol. 103, pp. 1852–1857, February 2006.

[5] M. Hoehn, E. Küstermann, J. Blunk, D. Wiedermann, T. Trapp, S. Wecker, M. Föcking, H. Arnold, J. Hescheler, B. K. Fleischmann, W. Schwindt, and C. Bührle, "Monitoring of implanted stem cell migration *in vivo*: A highly resolved *in vivo* magnetic resonance imaging investigation of experimental stroke in rats," *Proceedings of the National Academy of Sciences of the United States of America*, vol. 99, pp. 16267–16272, December 2002.

[6] R. A. Trivedi, J.-M. U-King-Im, M. J. Graves, J. J. Cross, J. Horsley, M. J. Goddard, J. N. Skepper, G. Quartey, E. Warburton, I. Joubert, L. Wang, P. J. Kirkpatrick, J. Brown, and J. H. Gillard, "In vivo detection of macrophages in human carotid atheroma: temporal dependence of ultrasmall superparamagnetic particles of iron oxide-enhanced MRI," *Stroke*, vol. 35, pp. 1631–1635, July 2004.

[7] M. Sirol, V. Fuster, J. J. Badimon, J. T. Fallon, P. R. Moreno, J.-F. Toussaint, and Z. A. Fayad, "Chronic thrombus detection with in vivo magnetic resonance imaging and a fibrin-targeted contrast agent," *Circulation*, vol. 112, pp. 1594–1600, November 2005.

[8] F. R. K. Chung, *Spectral Graph Theory*, vol. 92 of *CBMS Regional Conference Series in Mathematics*. American Mathematical Society, 1997.

[9] J. Cheeger, "A lower bound for the smallest eigenvalue of the Laplacian," in *Problems in Analysis* (R. C. Gunning, ed.), pp. 195–199, Princeton, NJ: Princeton University Press, 1970.

[10] M. Belkin and P. Niyogi, "Laplacian eigenmaps for dimensionality reduction and data representation," *Neural Computation*, vol. 15, pp. 1373–1396, June 2003.

[11] R. R. Coifman, S. Lafon, A. B. Lee, M. Maggioni, B. Nadler, F. Warner, and S. W. Zucker, "Geometric diffusions as a tool for harmonic analysis and structure definition of data: Diffusion maps," *Proceedings of the National Academy of Sciences of the United States of America*, vol. 102, pp. 7426–7431, May 2005.

[12] D. L. Donoho and C. Grimes, "Hessian eigenmaps: Locally linear embedding techniques for high-dimensional data," *Proceedings of the National Academy of Sciences of the United States of America*, vol. 100, pp. 5591–5596, May 2003.

[13] H.-H. Chang, J. M. F. Moura, Y. L. Wu, and C. Ho, "Immune cells detection of *in vivo* rejecting hearts in USPIO-enhanced magnetic resonance imaging," in *Proceedings of IEEE International Conference of Engineering in Medicine and Biology Society*, (New York, NY), pp. 1153–1156, August 2006.

[14] J. Shi and J. Malik, "Normalized cuts and image segmentation," *IEEE Transactions on Pattern Analysis and Machine Intelligence*, vol. 22, pp. 888–905, August 2000.

[15] R. O. Duda, P. E. Hart, and D. G. Stork, *Pattern Classification*. New York, NY: John Wiley & Sons, second ed., 2001.

[16] L. Grady and E. L. Schwartz, "Isoperimetric graph partitioning for image segmentation," *IEEE Transactions on Pattern Analysis and Machine Intelligence*, vol. 28, pp. 469–475, March 2006.

[17] S. Osher and J. A. Sethian, "Fronts propagating with curvature-dependent speed: Algorithms based on Hamilton–Jacobi formulations," *Journal of Computational Physics*, vol. 79, pp. 12–49, November 1988.

[18] J. A. Sethian, *Level Set Methods and Fast Marching Methods*. New York, NY: Cambridge University Press, second ed., 1999.

[19] C. Pluempitiwiriyawej, J. M. F. Moura, Y. L. Wu, and C. Ho, "STACS: New active contour scheme for cardiac MR image segmentation," *IEEE Transactions on Medical Imaging*, vol. 24, pp. 593–603, May 2005.

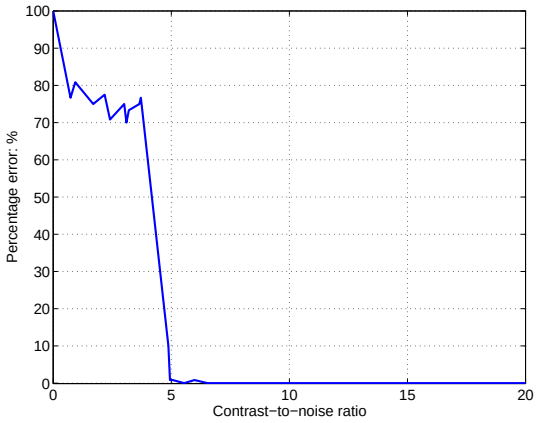

(a) Varied TE.

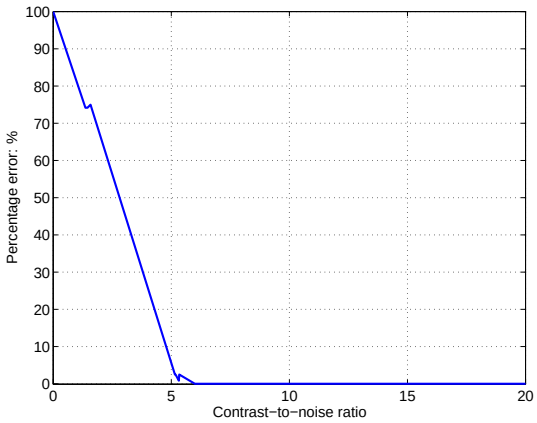

(b) Varied NEX.

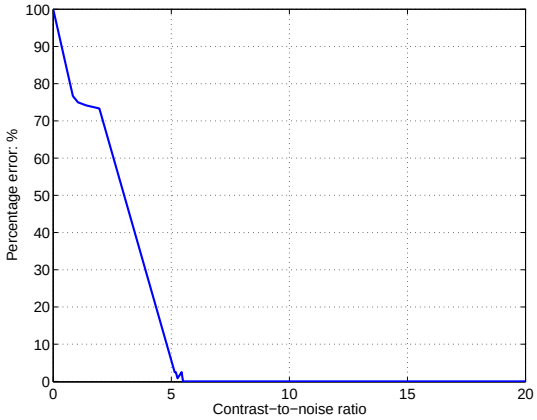

(c) Varied TR.

Fig. 4. Percentage error on phantom experiments by varying TE, NEX and TR.

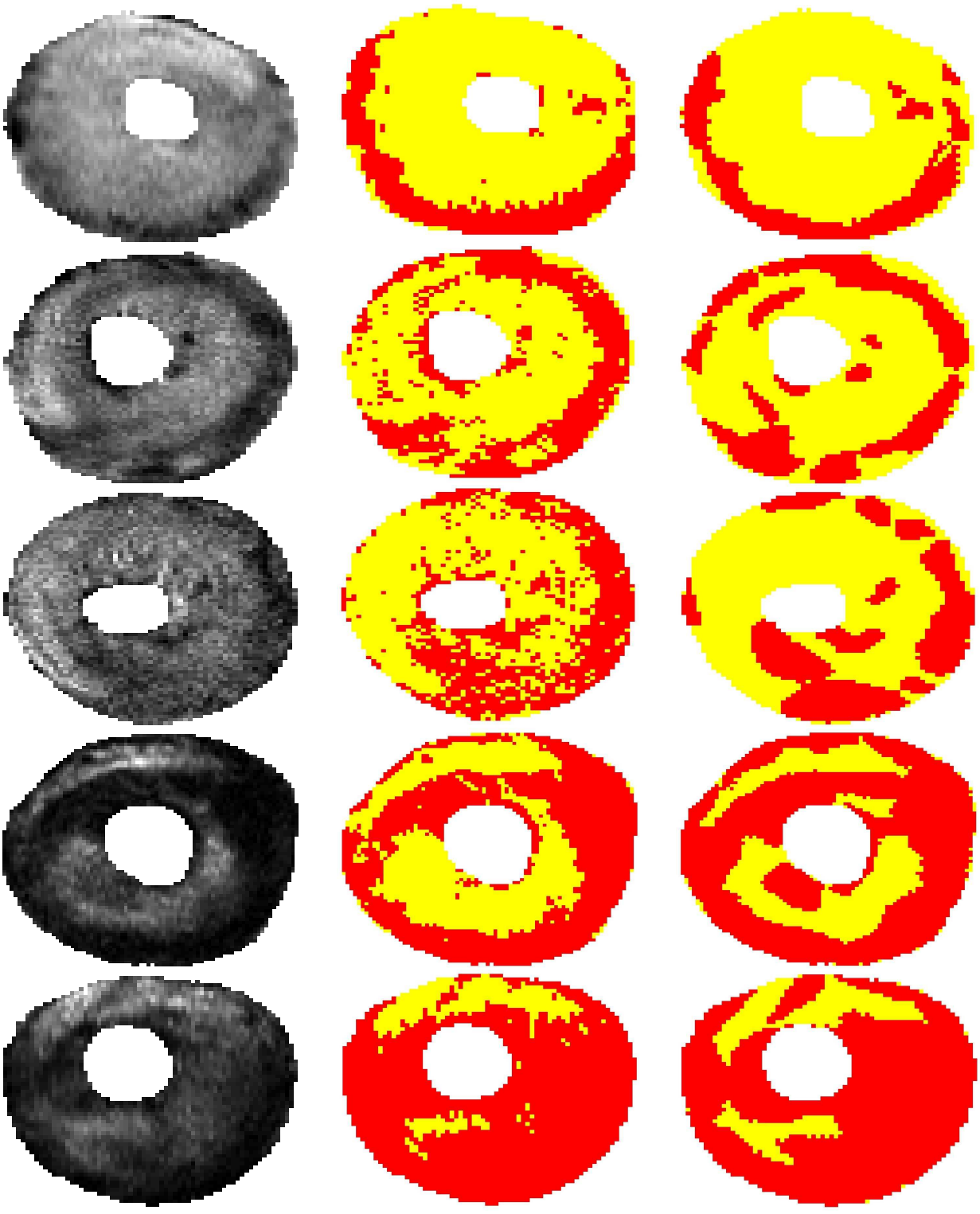

(a) USPIO-enhanced images. (b) Automatically classified results. (c) Manually classified results.

Fig. 5. Application of our algorithm to rejecting heart transplants. Red (darker) regions denote the classified USPIO-labeled pixels. Top to down: POD3, POD4, POD5, POD6, and POD7.

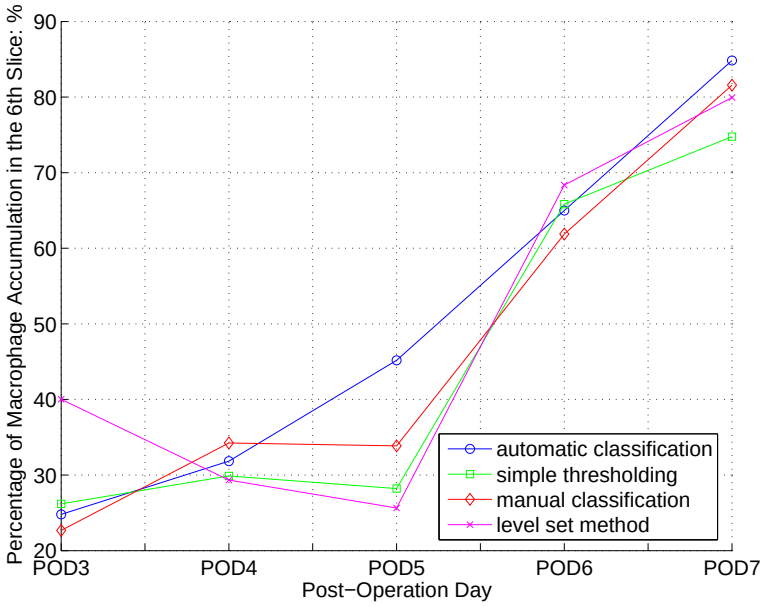

(a) Slice 6.

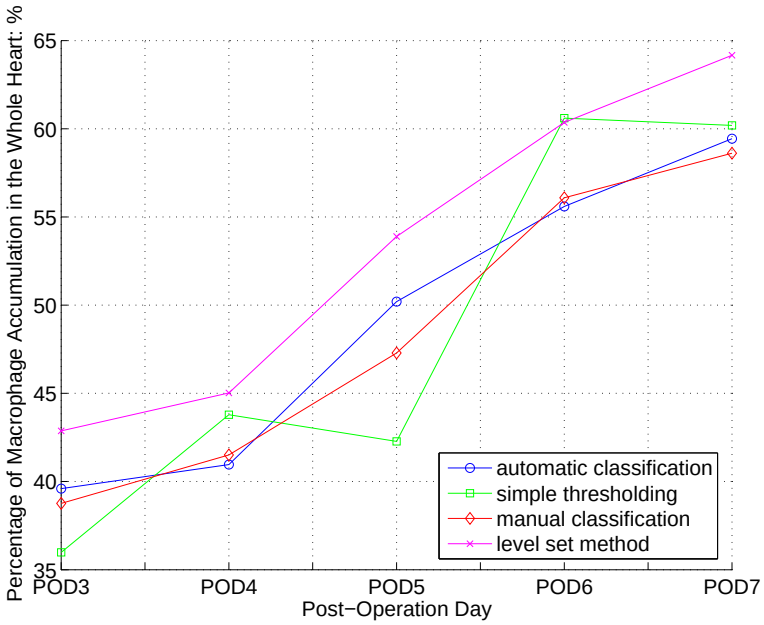

(b) Whole 3D heart.

Fig. 6. Immune cell accumulation of the heart transplants in Figure 5.

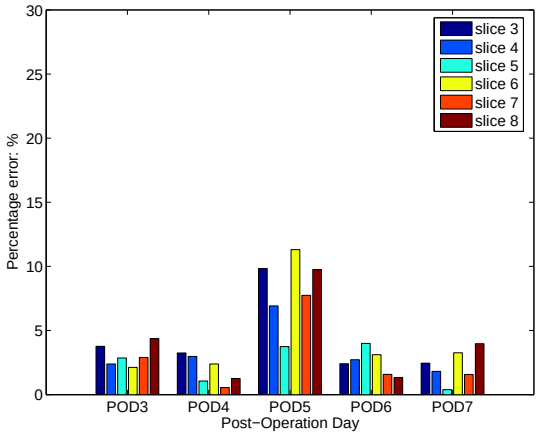

(a) Automatic classification proposed by this paper.

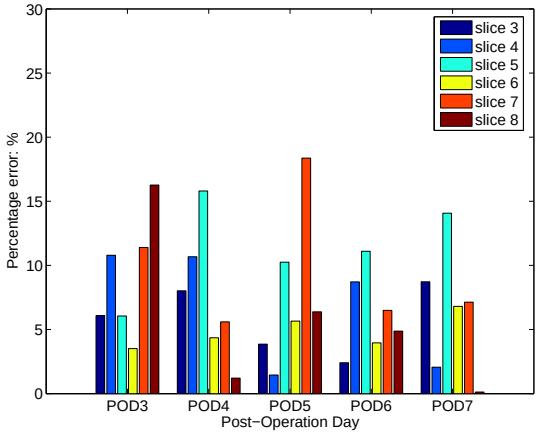

(b) Thresholding method.

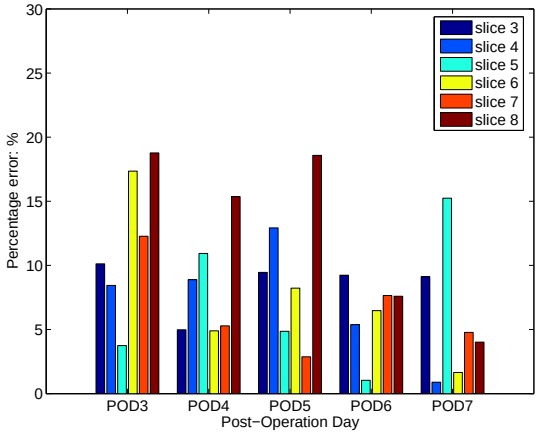

(c) Level set approach.

Fig. 7. Percentage deviation of various algorithms versus manual classification results.

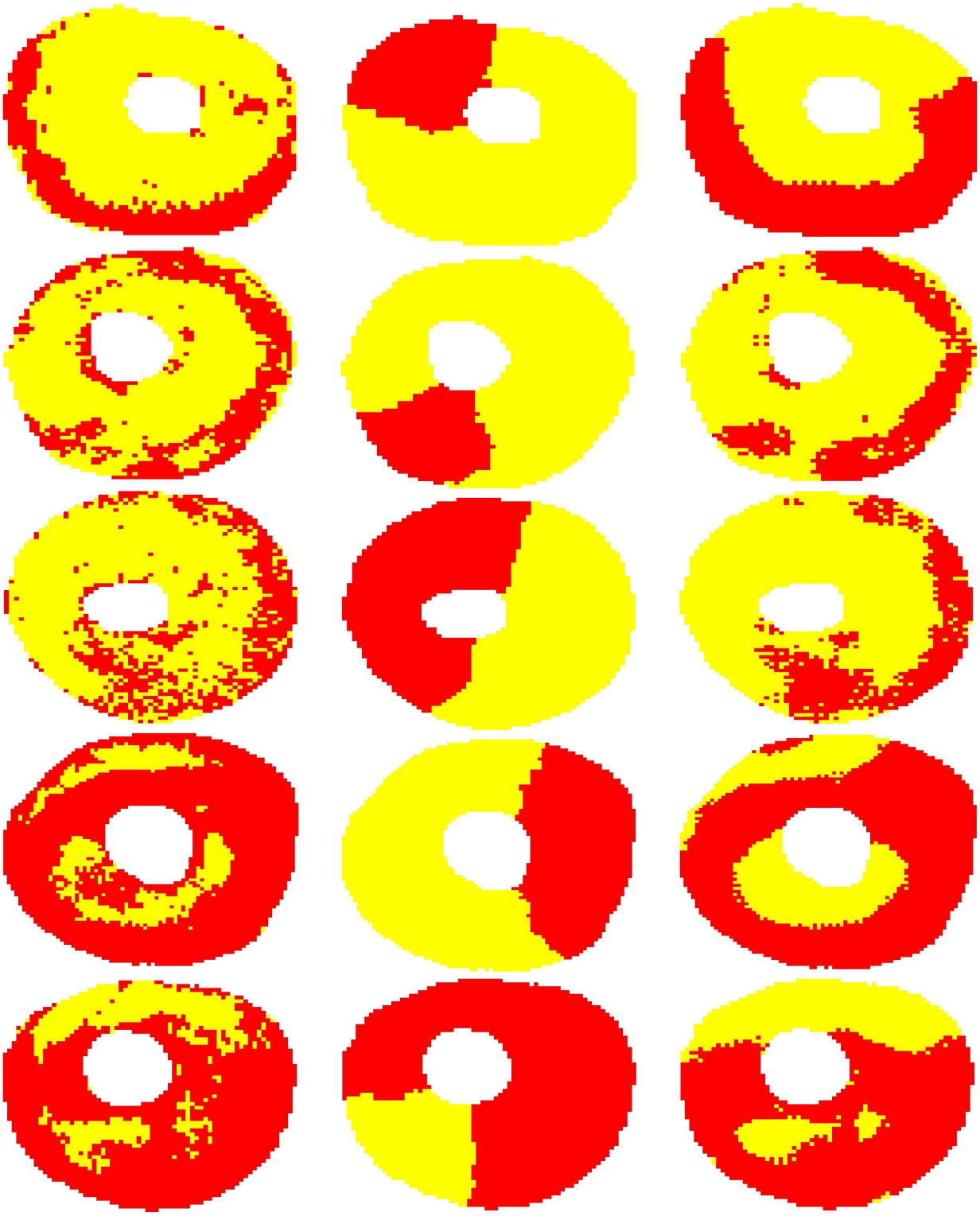

(a) Thresholding method. (b) Isoperimetric algorithm. (c) Level set approach.

Fig. 8. Application of other algorithms to rejecting heart transplants. Red (darker) regions denote the classified USPIO-labeled pixels. Top to down: POD3, POD4, POD5, POD6, and POD7.